JOURNAL OF GEOPHYSICAL RESEARCH, VOL. 116, B10101, doi:10.1029/2011JB008292, 2011

Anatomy of a pressure-induced, ferromagnetic-to-paramagnetic transition in pyrrhotite: Implications for the formation pressure of diamonds

Stuart A. Gilder,[1] Ramon Egli,[1] Rupert Hochleitner,[2] Sophie C. Roud,[1] Michael W. R. Volk,[1] Maxime Le Goff,[3] and Maarten de Wit[4,5]

Received 7 February 2011; revised 10 May 2011; accepted 18 July 2011; published 4 October 2011.

[1] Meteorites and diamonds encounter high pressures during their formation or subsequent evolution. These materials commonly contain magnetic inclusions of pyrrhotite. Because magnetic properties are sensitive to strain, pyrrhotite can potentially record the shock or formation pressures of its host. Moreover, pyrrhotite undergoes a pressure-induced phase transition between 1.6 and 6.2 GPa, but the magnetic signature of this transition is poorly known. Here we report room temperature magnetic measurements on multidomain and single-domain pyrrhotite under nonhydrostatic pressure. Magnetic remanence in single-domain pyrrhotite is largely insensitive to pressure until 2 GPa, whereas the remanence of multidomain pyrrhotite increases 50% over that of initial conditions by 2 GPa, and then decreases until only 33% of the original remanence remains by 4.5 GPa. In contrast, magnetic coercivity increases with increasing pressure to 4.5 GPa. Below ~1.5 GPa, multidomain pyrrhotite obeys Néel theory with a positive correlation between coercivity and remanence; above ~1.5 GPa, it behaves single domain–like yet distinctly different from uncompressed single-domain pyrrhotite. The ratio of magnetic coercivity and remanence follows a logarithmic law with respect to pressure, which can potentially be used as a geobarometer. Owing to the greater thermal expansion of pyrrhotite with respect to diamond, pyrrhotite inclusions in diamonds experience a confining pressure at Earth's surface. Applying our experimentally derived magnetic geobarometer to pyrrhotite-bearing diamonds from Botswana and the Central African Republic suggests the pressures of the pyrrhotite inclusions in the diamonds range from 1.3 to 2.1 GPa. These overpressures constrain the mantle source pressures from 5.4 to 9.5 GPa, depending on which bulk modulus and thermal expansion coefficients of the two phases are used.

Citation: Gilder, S. A., R. Egli, R. Hochleitner, S. C. Roud, M. W. R. Volk, M. Le Goff, and M. de Wit (2011), Anatomy of a pressure-induced, ferromagnetic-to-paramagnetic transition in pyrrhotite: Implications for the formation pressure of diamonds, *J. Geophys. Res.*, *116*, B10101, doi:10.1029/2011JB008292.

1. Introduction

[2] Pyrrhotite, an iron sulphide represented by the chemical formula $Fe_{1-x}S$ ($0.08 < x < 0.125$), is found in a wide range of natural environments such as mafic igneous and contact metamorphic rocks [*Hurlbut and Klein*, 1977] and meteorites [*Buddhue*, 1945; *Collinson*, 1986; *Rochette et al.*, 2005]. When $x = 0$, the mineral (troilite) is hexagonal with the niccolite (NiAs) structure; with higher x values, a deficiency in Fe with respect to S creates vacancies whose arrangement in the crystal lattice depends on the Fe concentration [*Laves*, 1930]. In a combined study of chemical and X-ray diffraction analyses of 82 natural pyrrhotites, *Arnold* [1967] found a gap in atomic Fe percentage between 49.8% (~FeS) and 48.1% (~$Fe_{11}S_{12}$). With decreasing amounts of Fe, the data chronicle a continuum of compositions ranging from $Fe_{11}S_{12}$ (47.8% Fe) to Fe_9S_{10} (47.3% Fe), a gap in compositions from ~47.3% to 46.6% Fe, and then a number of samples whose compositions narrowly distribute at Fe_7S_8 (46.6% Fe) [*Arnold*, 1967]. Pyrrhotite with compositions ranging from $Fe_{11}S_{12}$ to Fe_9S_{10} is hexagonal while Fe_7S_8 is monoclinic; 73% of the 82 natural pyrrhotite samples analyzed by *Arnold* [1967] contain mixtures of hexagonal and monoclinic phases.

[1]Department of Earth and Environmental Sciences, Ludwig Maximilians University, Munich, Germany.
[2]Mineralogische Staatssammlung München, Munich, Germany.
[3]Laboratoire du Paléomagnétisme, Institut de Physique du Globe, Paris, France.
[4]AEON, Department of Geological Sciences, University of Cape Town, Rondebosch, South Africa.
[5]Now at Africa Earth Observatory Network, Nelson Mandela Metropolitan University, Port Elizabeth, South Africa.

0148-0227/11/2011JB008292

[3] Hexagonal pyrrhotite is antiferromagnetic and the monoclinic phase is ferromagnetic with a Curie temperature of about 325°C, depending on the composition [e.g., *Haraldsen*, 1937, 1941; *Néel*, 1952]. The ferromagnetic character of monoclinic pyrrhotite arises from the regular ordering of vacancies on alternate basal layers in an otherwise antiferromagnetic lattice [*Néel*, 1952; *Bertaut*, 1953; *Vaughan and Ridout*, 1970; *Schwarz and Vaughan*, 1972]. Layers containing vacancies have one-fourth fewer Fe atoms, so that alternating fully filled and partially filled layers produce an imbalance that yields a net magnetization. Hexagonal pyrrhotite also has alternate layers of vacancy-filled and vacancy-free layers, but the stacking yields no inequality of moments in the magnetic sublattices, thereby remaining in the antiferromagnetic state. A rearrangement of the vacancies beginning at ~220°C turns the hexagonal phase ferromagnetic [*Haraldsen*, 1937; *Hayase et al.*, 1963; *Morimoto et al.*, 1975; *Zapletal*, 1993]. This is called the lambda transition due to a peak in magnetization or susceptibility at ~240°C.

[4] A concerted effort has gone into characterizing the magnetic properties of pyrrhotite. Vacancy ordering produces crystalline anisotropy [*Bin and Pauthenet*, 1963] that confines the spontaneous moment to the basal plane, perpendicular to the *c* axis [*Rochette et al.*, 1990; *Kamimura et al.*, 1992]. The basal plane anisotropy is uniaxial, with multidomain grains being dominated by parallel 180° walls and rare closure domains [*Halgedahl and Fuller*, 1981; *Soffel*, 1981]. Initial susceptibility, including its frequency and field-strength dependencies, thermoremanent magnetization intensity and the ratio of the coercivity of remanence (Bcr) to magnetic coercivity (Bc) all vary with grain size [*Dekkers*, 1988, 1989; *Worm et al.*, 1993].

[5] Of particular interest here is that pyrrhotite undergoes a magnetic phase transition under pressure, as first noticed when Mössbauer spectra of synthetic Fe_7S_8 became paramagnetic at 1.6 GPa [*Vaughan and Tossell*, 1973]. Shock and release wave data on three natural pyrrhotites delineated a phase change at 2.7 to 3.8 GPa [*Ahrens*, 1979]. X-ray diffraction of Fe_7S_8 using a 4:1 methanol-ethanol pressure transmitting medium indicates a phase transition at ~6.2 GPa marked by a reduction in *c* axis lattice spacing with little change along the *a* axis [*Kamimura et al.*, 1992]. *Kamimura et al.* [1992] concluded that the *c* axis lattice spacing likely governs the magnetic and electrical properties of pyrrhotite. Further high-pressure work using Mössbauer spectroscopy and X-ray diffraction found that pyrrhotite goes to a paramagnetic state at 4.5 ± 0.5 GPa [*Kobayashi et al.*, 1997], where the electronic bandwidth increases enough to induce a metallic state and collapse iron's magnetic moment. Using neutron diffraction, *Rochette et al.* [2003] found that the intensity of the (001) ferromagnetic peak decreases with pressure until the signal vanishes between 2.6 and 3.1 GPa. Experiments on pyrrhotite using both static and shock pressures show some discrepancy. Static stress linearly decreased the magnetic moment until full demagnetization at 2.8 GPa [*Rochette et al.*, 2003; *Bezaeva et al.*, 2010], while shock pressures up to 12 GPa demagnetized the original remanence by 40% to 90%, with the exception of two of 16 samples whose remanence increased to levels exceeding those of the preshocked remanence [*Louzada et al.*, 2007, 2010].

[6] Until now, direct measurements of the magnetic properties of pyrrhotite under pressure have not been reported. Such data are important for furthering our knowledge of Martian magnetic anomalies, where pyrrhotite is a candidate magnetic mineral [*Dunlop and Arkani-Hamed*, 2005], and for the magnetic histories of meteorites [e.g., *Rochette et al.*, 2005]. In addition, diamonds sometimes contain pyrrhotite inclusions, and because of the high differential thermal expansion between pyrrhotite and diamond, pyrrhotite may be under a high confining pressure on Earth's surface when coming from great depth [*Clement et al.*, 2008]. Thus, the magnetic properties of pyrrhotite could potentially be used as a geobarometer for the host diamond. For these reasons, we carried out a study on pyrrhotite to quantify its magnetic characteristics under pressure and better describe the magnetic signature of a pressure-induced phase transition. Our findings suggest that source-pressure estimates on minerals bearing pyrrhotite inclusions can be obtained using nondestructive magnetic techniques that require minimal sample preparation.

2. Sample Description

[7] The Munich Mineralogical State Collection (Mineralogische Staatssammlung München) provided us with several natural pyrrhotite samples, each greater than 1 cm in diameter. After running a suite of characterization analyses (at Ludwig Maximilians University, Munich, unless otherwise specified) described below, we chose two (MSM73410 from Schmiedeberg, Germany and MSM73409 from Colquiri, Bolivia) for our high-pressure study. Chemical compositions were determined using a Camebax SX100 electron microprobe operating with an acceleration voltage of 15 keV and 20 nA beam current. Standards included synthetic periclase (Mg), hematite (Fe), sphalerite (ZnS), GaAs (As) and NiO (Ni) and natural ilmenite (Mn, Ti) with a reproducibility to >99% for each element (Table 1). The matrix correction followed the procedure of *Pouchou and Pichoir* [1984]. Both samples have detectable amounts of As and Ni and lack traces of Mn, Zn, Cu, Ti and Mg; MSM73410 has a lower Fe:S ratio than MSM73409. We measured X-ray powder diffraction using a Philips Xpert X-ray diffractometer with CuKα X-radiation between 2Θ = 5–75° operating at 40 kV and 30 mA (Table 1). Synthetic Si served as an internal standard. Data were processed with the RMSKempten ADM software package.

[8] Figures 1a and 1b show ambient pressure thermomagnetic curves and the derivatives of those curves obtained with a Petersen Instruments, variable field translation balance when heating at 30°/minute to ~400°C (absolute accuracy ~±5°C) in air with a 30 mT direct current field. MSM73410 has a single Curie temperature at 322°C, indicative of monoclinic pyrrhotite, while MSM73409 displays both a lambda transition with a maximum at 245°C and a Curie temperature at 324°C, typical of mixed monoclinic and hexagonal phases. Curie point and chemical data are thus compatible for both samples. Magnetization above the Curie temperature is negligible, which implies that magnetic phases with Curie temperatures higher than 325°C are absent (i.e., no maghemite, magnetite, hematite, etc.). Hysteresis loops of MSM73410 and MSM73409 exhibit more multidomain-like and single-domain-like character,

Table 1. Average Chemical and Unit Cell Parameters of the Pyrrhotite Samples Used in This Study

Element	MSM73410 $n = 16$[a]	Standard Deviation[b]	MSM73409 $n = 15$[a]	Standard Deviation[b]
As	0.036	0.023	0.025	0.022
S	**39.595**	**0.405**	**38.737**	**0.203**
Mn	BD[c]		BD	
Zn	BD		BD	
Fe	**59.962**	**0.376**	**60.821**	**0.243**
Cu	BD		BD	
Ti	BD		BD	
Mg	BD		BD	
Ni	0.029	0.023	0.063	0.032
Total	**99.696**	**0.581**	**99.645**	**0.274**
$Fe_{1-x}S$	$Fe_{0.87}S$	Standard Deviation[b]	$Fe_{0.90}S$	Standard Deviation[b]
a, Å	12.794	0.007	12.807	0.002
b, Å	6.882	0.002	6.871	0.002
c, Å	11.879	0.004	11.886	0.004
β, °	90.931	0.005	90.921	0.002
Vol., $Å^3$	1045.87		1045.87	
c/a	0.92843		0.92804	

[a]Here n represents the number of analyses. Pyrite was separated from MSM73410 before the X-ray diffraction analyses. For MSM73409, X-ray and chemical data are an average of both pyrrhotite phases.
[b]One standard deviation about the mean value.
[c]BD, below detection limits.

respectively (Figures 1c and 1d). The remanence ratio (remanent saturation magnetization (Mrs)/saturation magnetization (Ms)) and the coercivity ratio (Bcr/Bc) are 0.18 and 1.33 for MSM73410 and 0.44 and 1.21 for MSM73409. As the samples used in these experiments consist of several millimeter-sized pieces, the single-domain character of MSM73409 likely results from a fine-scale intergrowth of two phases, as is common in natural, two phase pyrrhotites [see *Arnold*, 1967, Figure 2].

[9] We measured the Mössbauer spectra of each sample with a 512 multichannel analyzer and a constant acceleration drive with no applied field at room temperature (Figures 1e and 1f). The commercial "Recoil" software by Lagarec and Rancourt was used for line fitting using 4 sextets (2:1:2:2). Isomer shift data are in reference to metallic Fe with absorber thicknesses <5 mg Fe/cm^2. MSM73410 has hyperfine parameters of: center shift (δ) = 0.67, 0.69, 0.66, 0.68 mm/s, quadrupole splitting (2ε) = 0.02, 0.15, 0.08, 0.10 mm/s and the hyperfine field (B_{HF}) = 30.6, 29.3, 25.2, 22.7 T. A paramagnetic contribution from pyrite is also discernable (Figure 1e). The hyperfine parameters for MSM73409 are δ = 0.70, 0.72, 0.70, 0.69 mm/s, 2ε = 0.08, 0.04, 0.09, 0.22 mm/s, and B_{HF} = 29.9, 27.6, 25.7, 23.5 T. These results agree with Mössbauer spectra of other pyrrhotite [e.g., *Jeandey et al.*, 1991] and they reveal no other ferromagnetic phase.

[10] We also measured the magnetic moment of the samples between 10 K and room temperature at ambient pressure using a Quantum Design, magnetic property measurement systems at the Institute de Physique du Globe de Paris (MSM73410) and at the Universität Bremen (MSM73409; see Figures 1g and 1h). The experimental protocol was to cool the samples from 300 K to 10 K in either a zero field (ZFC in Figure 1) or in a 2.5 T field (FC in Figure 1), apply a 2.5 T field at 10 K, and then to measure the magnetic moment in a null field upon warming from 10 K to 300 K. Both samples display a sharp drop in magnetization around 35 K, indicative of pyrrhotite [*Dekkers et al.*, 1989; *Rochette et al.*, 1990]; no other break in slope occurred above 35 K. Taken together, the analytical results show that pyrrhotite comprises the only source of magnetic remanence in our samples, with no contribution from other magnetic minerals. MSM73410 consists of pure monoclinic Fe_7S_8 whereas MSM73409 has monoclinic and hexagonal phases.

3. Experimental Procedure and Results

[11] In a miniature moissanite anvil cell, we loaded several tens of polycrystalline grains, whose sizes generally ranged from 20 to 100 μm, of either MSM73410 or MSM73409 together with a few ruby chips and silica gel in an ~400 μm diameter hole in a work-hardened Bronze-Be gasket. The cell was placed into the bore of a 2G Inc., three axis, superconducting (SQUID) magnetometer (Ludwig Maximilians Universität-Munich) where the full magnetic vector was measured four times by rotating the cell about its three orthogonal axes. The average moment and its angular uncertainty were calculated after accounting for the magnetization of the sample handler and the empty cell (further details are available in the work of *Gilder et al.* [2004] and *Gilder and Le Goff* [2008]). Pressure was measured directly in the cell before and after each experiment using ruby fluorescence spectroscopy [*Adams et al.*, 1976; *Chervin et al.*, 2001] with a Princeton Instruments (PIXIS) charged coupled device connected to a 150 mm, ARC SpectraPro spectrograph. Pressure was monitored using two rubies, one placed near the center of the cell and one near the edge, to monitor potential pressure gradients. Distinctly separate R1 and R2 spectral peaks suggest pressure conditions were hydrostatic except when noted in Table 2, which lists the maximum pressure and the average pressure in the cell assuming a parabolic pressure profile. Data presented below consider the average pressure. Five separate experiments were carried out—two on MSM73410 and three on MSM73409.

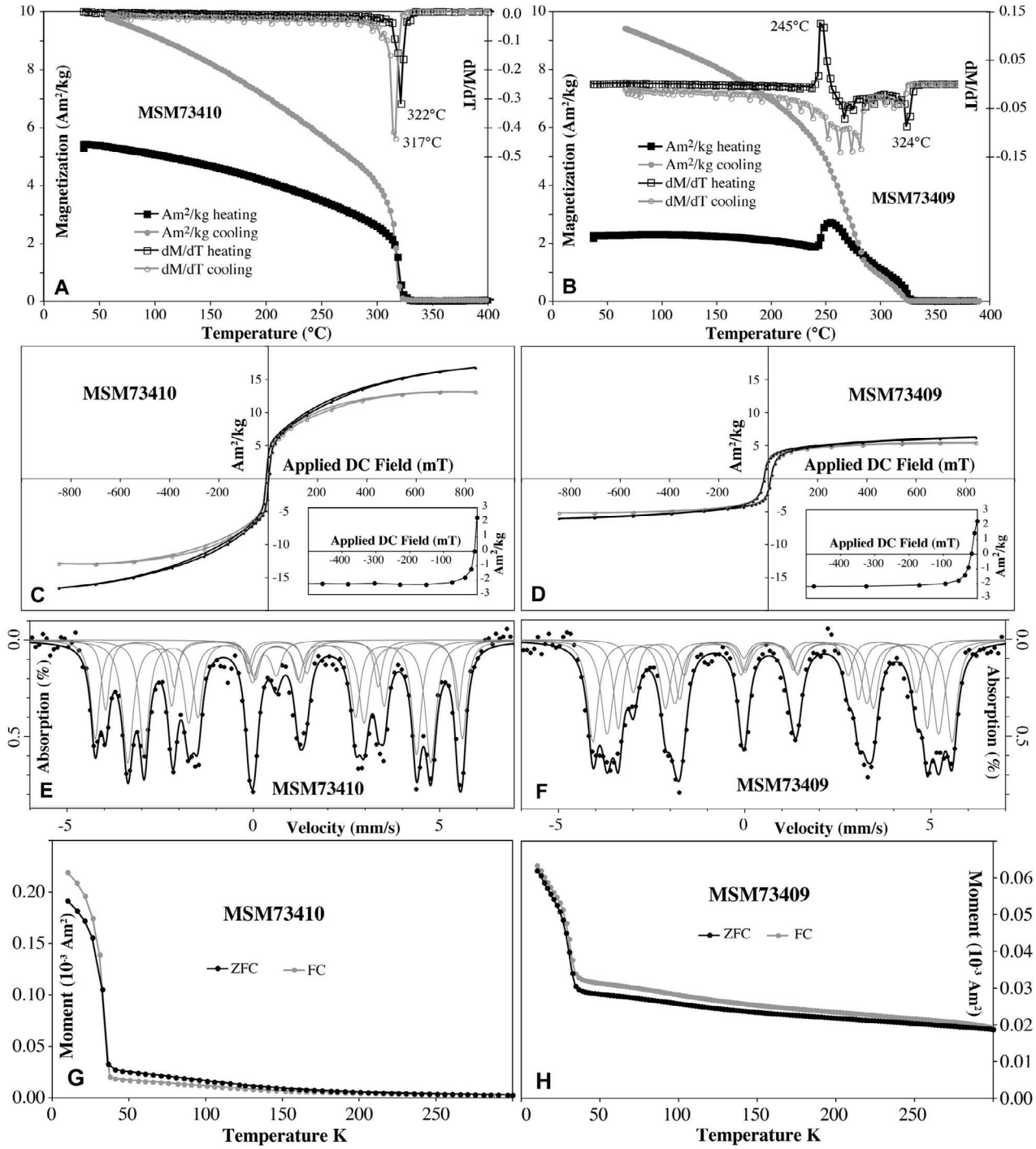

Figure 1. Magnetic characterization of the two pyrrhotite samples used in this study. (a and b) In-field magnetization measured as a function of temperature. (c and d) Raw (black curves) and corrected (gray curves) hysteresis loops; insets are backfield acquisition curves. (e and f) Mössbauer spectra; see text for discussion. (g and h) Magnetic moments measured below room temperature when cooling from room temperature to 10 K in a null or zero (ZFC) or 2.5 T (FC) applied field. All curves show a transition at ~35 K, typical of pyrrhotite.

[12] At successive pressure steps, we measured the stepwise acquisition of isothermal remanent magnetization, applied perpendicular to the axis of the moissanite pistons, using an electromagnet whose pole pieces slide through the cell's housing until they abut the pistons. First we applied a magnetization of 370 mT in the $+y$ axis direction, and then incrementally increased the applied field strength in the $-y$ axis direction until reaching 370 mT. Figure 2a shows an example for run MSM73410-20081215, where one observes that the magnetization becomes saturated (moment

Table 2. Summary of the Results From This Study[a]

Peak Pressure (GPa)	Mean Pressure (GPa)	SIRM (Am^2)	Standard Deviation[b] (Am^2)	Bcr (mT)	MDF (mT)
		MSM73410-20080805			
0.00	0.00	5.65E-08	4.87E-09	11.8	–
0.38	0.38	6.36E-08	5.94E-09	13.5	9.8
1.29	1.29	8.73E-08	4.21E-09	24.0	15.4
2.39	2.31	9.58E-08	2.77E-09	53.5	33.8
2.96[c]	2.56[c]	1.01E-07	7.10E-09	65.0	48.9
0.84	0.79	1.01E-07	7.08E-09	24.7	14.2
0.00	0.00	9.86E-08	5.45E-09	19.5	13.1
		MSM73410-20081215			
0.00	0.00	9.73E-08	1.76E-09	14.8	7.9
1.50	1.44	1.61E-07	1.92E-09	34.2	17.9
2.42	2.32	1.57E-07	2.73E-09	73.8	45.0
3.08	2.88	1.54E-07	2.19E-09	89.5	66.4
3.68	3.45	1.25E-07	3.22E-09	100.0	99.3
4.27	4.09	5.88E-08	1.89E-09	118.2	130.8
4.67	4.54	2.88E-08	1.11E-09	117.2	95.8
4.06	3.98	4.81E-08	1.47E-09	117.4	148.0
3.49	3.49	9.14E-08	1.97E-09	107.7	125.8
2.91	2.91	1.44E-07	1.96E-09	96.6	104.1
2.10	2.03	1.94E-07	2.34E-09	67.8	55.9
0.63	0.62	2.11E-07	8.35E-10	36.2	22.5
0.00	0.00	2.19E-07	9.07E-10	34.6	21.4
		MSM73409-20080806			
0.00	0.00	9.11E-08	4.24E-09	18.5	12.6
0.36	0.36	9.07E-08	4.33E-09	19.7	13.4
1.02	0.97	1.11E-07	7.44E-09	28.0	17.1
1.70	1.63	1.13E-07	7.58E-09	43.2	33.5
2.33[d]	2.17	1.11E-07	7.86E-09	63.8	50.1
		MSM73409-20080810			
0.00	0.00	1.14E-07	8.22E-09	23.3	11.1
0.81	0.81	1.25E-07	3.65E-09	35.4	22.0
1.73	1.57	1.28E-07	1.94E-09	53.5	32.4
2.57	2.33	1.23E-07	3.23E-09	75.2	47.1
3.25[d]	2.88	1.13E-07	8.45E-09	86.1	48.4
		MSM73409-20081218			
0.00	0.00	1.47E-07	2.44E-09	19.5	10.9
1.17	1.10	1.45E-07	2.38E-09	35.8	21.0
1.99	1.73	1.49E-07	2.88E-09	55.9	35.6
2.66	2.16	1.51E-07	2.04E-09	74.6	50.2
3.21	2.51	1.36E-07	2.37E-09	96.9	58.7
3.87	2.95	1.27E-07	3.09E-09	101.5	75.1
2.47	2.00	1.56E-07	4.56E-09	80.1	56.7
0.00	0.00	1.76E-07	2.00E-09	47.4	31.2

[a]Abbreviations are as follows: SIRM, saturation isothermal remanent magnetization; Bcr, coercivity of remanence; MDF, median destructive field.
[b]One standard deviation about the mean.
[c]R1 and R2 peaks indicate nonhydrostatic behavior.
[d]Cell failed when compressing to the next pressure step, no decompression measurements; note that pressure path goes from top to bottom of each list.

at −370 mT = moment at +370 mT and equivalence of moments over last few steps) at high magnetic fields for all pressures. From these experiments we calculated the average and standard deviation of the saturation isothermal remanent magnetization (SIRM) from the magnetic moments of the last three steps at each pressure interval, together with the coercivity of remanence (Bcr), defined as the magnetic field required to null the remanent magnetization (Table 2). After completing each acquisition curve, the sample underwent stepwise alternating field demagnetization up to 190 mT (Figure 2b). These experiments enabled us to determine the median destructive field (MDF; see Table 2), which is the peak applied field in mT needed to demagnetize 50% of the initial magnetization. Using the experimental data of *Dekkers* [1988] from magnetite-free pyrrhotite combined with the theory of *Dankers* [1981] shows that MDF is linearly related to the bulk coercive force (Bc, in mT) in pyrrhotite for a wide range of grain sizes.

[13] Figure 3a plots the SIRM moments upon increasing pressure for all five experiments. The variability between the runs for each species arises because there is no way to normalize the data by volume or mass. We thus normalized the values of each run with respect to its initial (zero) pressure value. Seen in this way (Figure 3b), the SIRM curves appear more coherent for each sample, with the multidomain-rich sample (MSM73410) gaining about 50% more magnetization by 2 GPa than the more single-domain-rich sample (MSM73409). Above ~2.5 GPa, SIRM begins to decrease until only 33% of the original SIRM moment

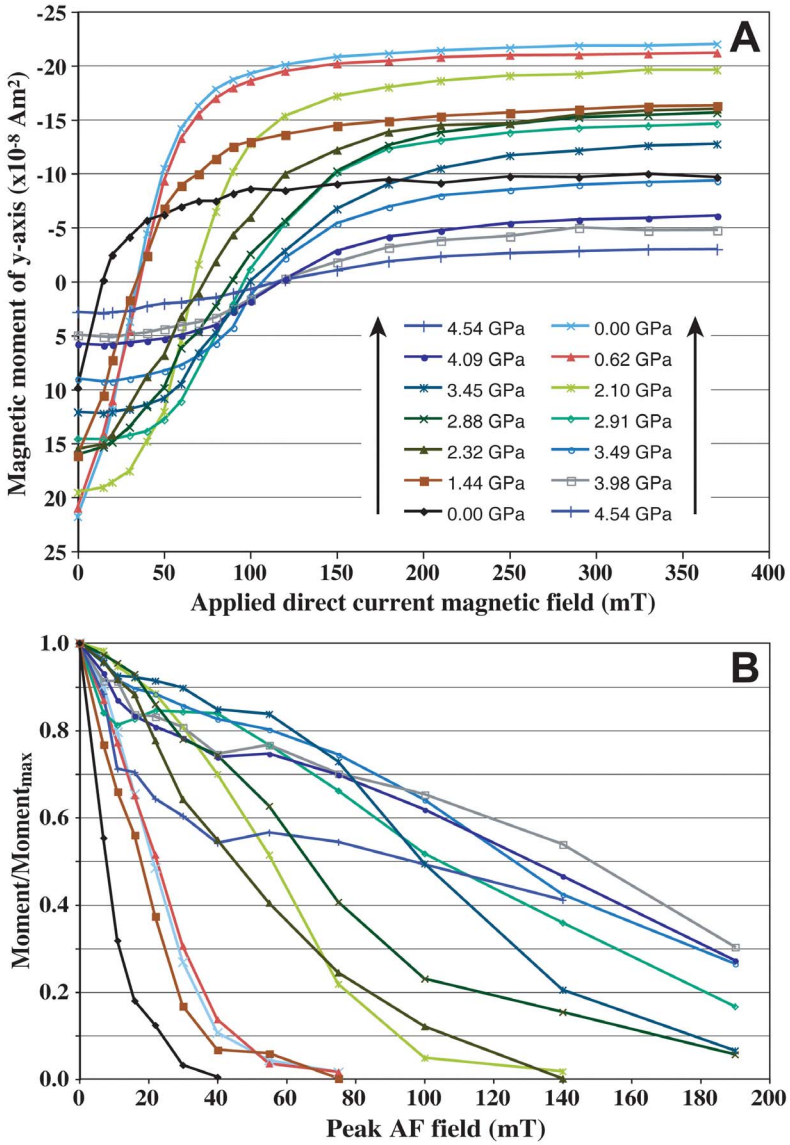

Figure 2. (a) Stepwise acquisition of isothermal remanent magnetization in the $-y$ axis direction after the application of a 370 mT field saturating magnetization in the $+y$ axis direction for sample MSM73410, experiment 20081215. Arrows indicate the compression-decompression path. (b) Stepwise alternating field (AF) demagnetization of the saturation isothermal remanent magnetization (SIRM) shown in Figure 2a at each pressure step. Magnetic moments are normalized with respect to the value of the starting SIRM at each pressure treatment. The median destructive field is the field (in mT) required to remove 50% of the original magnetization.

remains by 4.5 GPa. Further compression was useless as the SIRM moment measured in the 4.54 GPa experiment was within the uncertainties of correcting for the moment of the empty cell. Upon full decompression (Figure 3c), SIRM moments are 20 to 125% higher than the initial value, with the multidomain grains having greater SIRM moments than single-domain grains; the SIRM moment at full decompression is greater for the multidomain sample exposed to higher pressure. *Louzada et al.* [2007] also observed enhanced SIRM for shocked pyrrhotite relative to the pre-shocked value.

[14] Figure 3d plots Bcr upon increasing pressure for all five experiments. Normalization is not an issue for Bcr and MDF as it is for SIRM. The average initial Bcr of MSM73410 (13.3 mT) and MSM73409 (20.4 mT) compare relatively well with that derived from the variable field translation balance (7.3 and 17.1 mT, respectively; see insets in Figures 1c and 1d). Likewise, the MDF data are quite compatible between the experiments as higher coercivities are again seen for the more single-domain-rich sample (MSM73409) than for the more multidomain-rich sample (MSM73410; see Figure 3e). Relative increases in Bcr and MDF are greater upon decompression than for SIRM (Figures 3f and 3g). Unlike SIRM, Bcr and MDF values upon full decompression are higher for the more single-domain-rich sample than for the more multidomain-rich

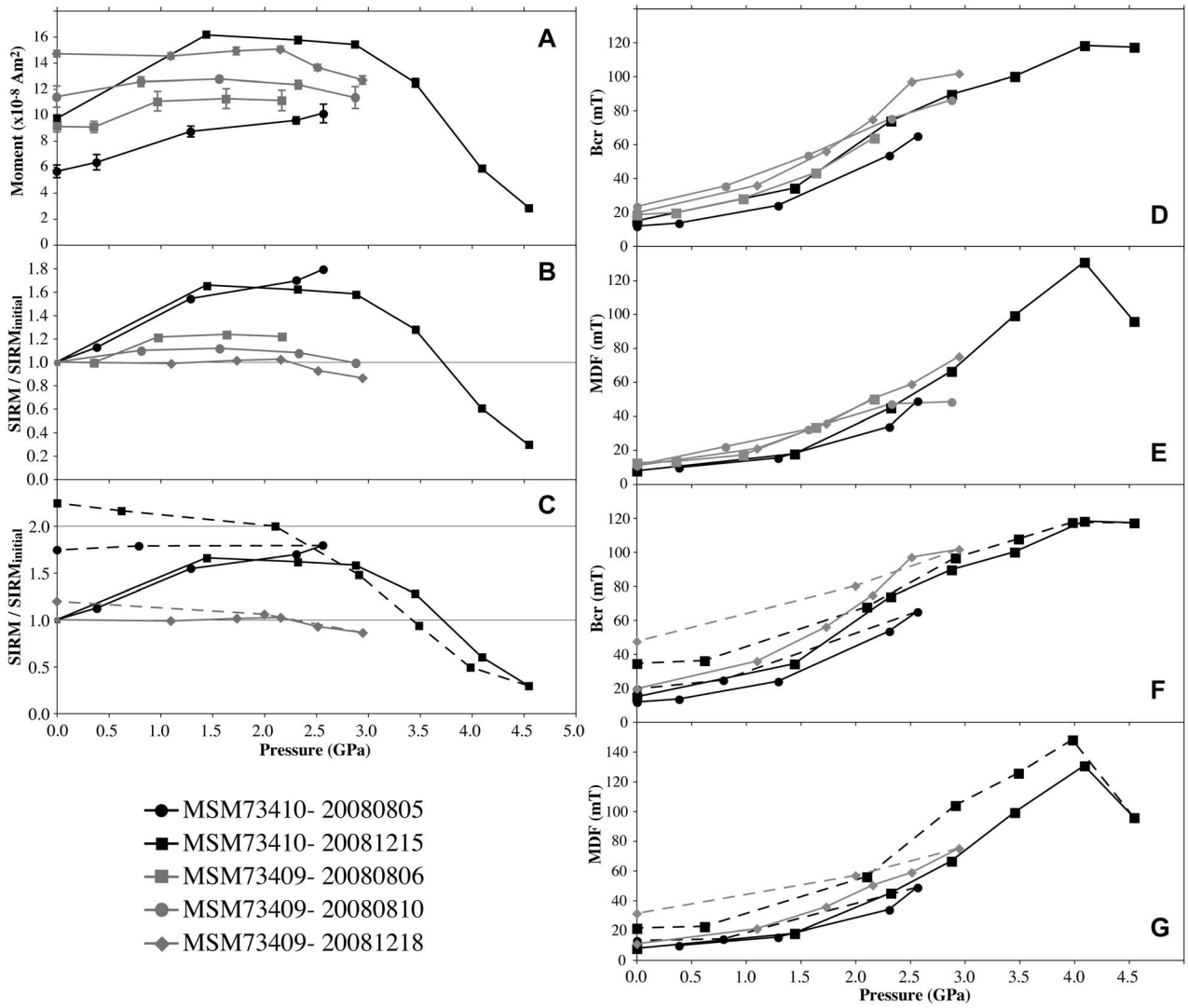

Figure 3. (a) Saturation isothermal remanent magnetization (SIRM) as a function of pressure (increasing path only). SIRM moments are the average of the last three backfield remagnetization field steps (1 σ uncertainties from Table 2). (b) SIRM normalized by the initial (P = 0) value as a function of pressure (increasing path only). (c) Same as Figure 3b, except the experiments with decompression paths are shown (dashed lines). (d) Coercivity of remanence (Bcr) as a function of pressure (increasing path only). (e) Median destructive field as a function of pressure (increasing path only). (f and g) Same as Figures 3d and 3e, except the experiments with decompression paths are shown (dashed lines).

sample. The coercivity ratio (Bcr/MDF) decreases by about a factor of two from 0 to 4 GPa and is roughly 15% lower upon full decompression than initial conditions. Higher coercivities were also observed for shocked pyrrhotite relative to the preshocked state [*Louzada et al.*, 2007].

[15] One must question how the degree of nonhydrostaticity bears on the results. Pressure gradients vary widely between experiments (Figure 4), with differences likely due to variable proportions of pyrrhotite to pressure medium, to precise location of the two rubies with respect to the center and edge of the cell, to potential interaction of the rubies with the pyrrhotite grains, moissanite cell or gasket, and/or to unequal cell dimensions. Moreover, the grain shapes are highly angular and irregular, plus they likely contain imperfections, so even perfectly hydrostatic pressure conditions would lead to a certain degree of nonuniform strain on the particles. Pressure gradients are generally lower upon decompression than upon compression. A comparison between Figures 3 and 4 reveals no obvious connection between pressure gradient and magnetic properties; for example, the degree of nonhydrostaticity does not significantly influence the general trend of the measurements. In other words, despite differences in measured pressure gradients ranging from 0.1 to >1.0 GPa over 200 microns among the various experiments, the magnetic results appear consistent (see Figures 3b, 3d, and 3e), which means that although nonhydrostatic stresses surely play a role in influencing the magnetic properties of pyrrhotite, the effect appears to be saturated at relatively low levels of nonhydrostaticity. We conclude that the observed changes in

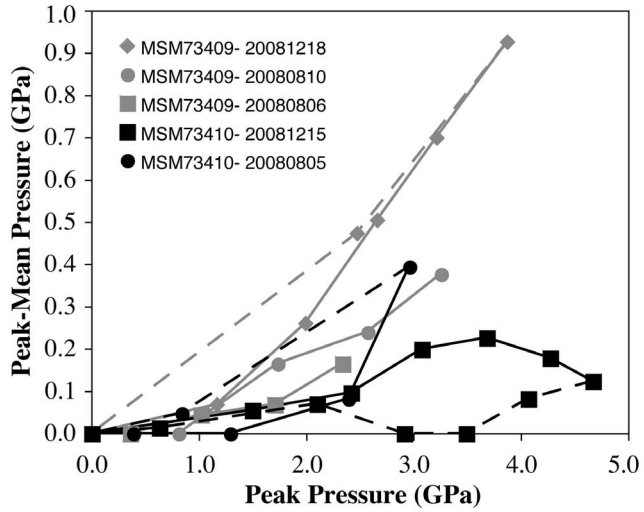

Figure 4. Peak pressure minus mean pressure as a function of peak pressure for all five experiments. Differences give an indication of the pressure gradient in the cell. Decompression paths are shown as dashed lines.

magnetic properties under such nonhydrostatic pressure conditions can be found in nature.

4. Magnetic Anatomy of a Pressure-Induced Phase Transition in Pyrrhotite

[16] This study has provided reproducible results for two pyrrhotite samples whose ferromagnetic component is distinguished primarily by magnetic domain state. For the multidomain sample, one clearly observes an increase in coercivity with pressure up until ~4.5 GPa (Figure 3). This increase in coercivity is paralleled by the single-domain sample up to the highest pressures achieved (3 GPa). The increase in coercivity in both the single-domain and multidomain pyrrhotite is likely explained by the relative change in *c*/*a* lattice spacing as a function of pressure [*Kamimura et al.*, 1992], which acts to increase the crystalline anisotropy and hence the magnetostrictive anisotropy and the coercivity. Domain wall pinning may also play a role, but one would then expect the coercivity of the multidomain sample to be more strain-sensitive and this does not appear to be the case. In other words, the similarity in coercivity increase between single-domain and multidomain samples

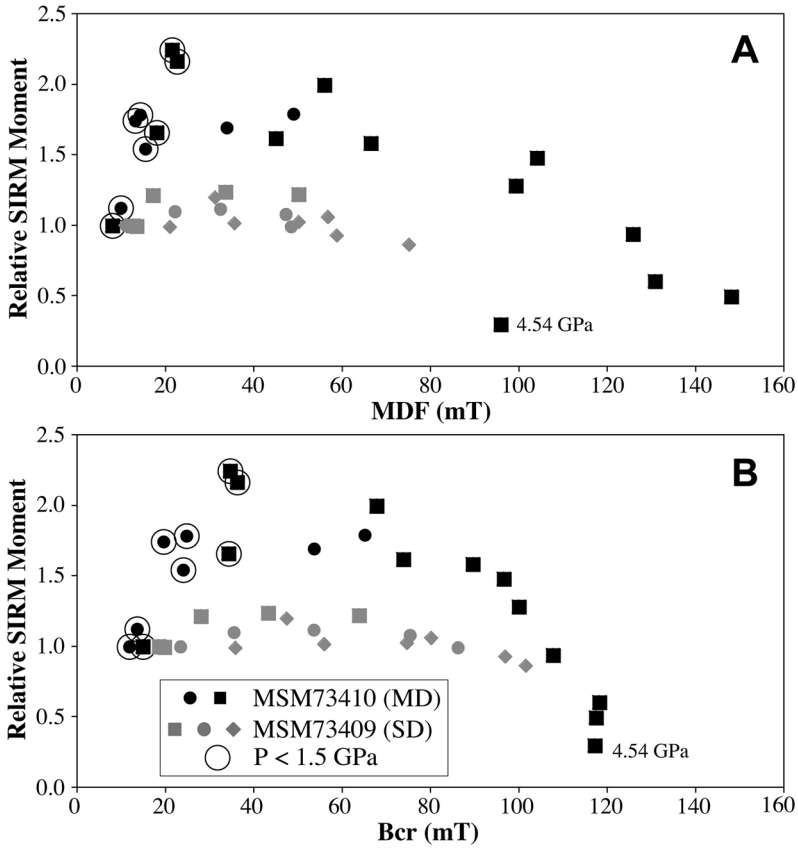

Figure 5. (a) Median destructive field (MDF) and (b) coercivity of remanence (Bcr) versus saturation isothermal remanent magnetization (SIRM) normalized by the initial (P = 0) value for all data in Table 2. Symbols are the same as in previous figures. Circled data are all points from the multidomain-rich sample obtained at pressures lower than 1.5 GPa. These points define a positive linear slope; points obtained at pressures between 2.8 and 4.5 GPa define a negative linear slope.

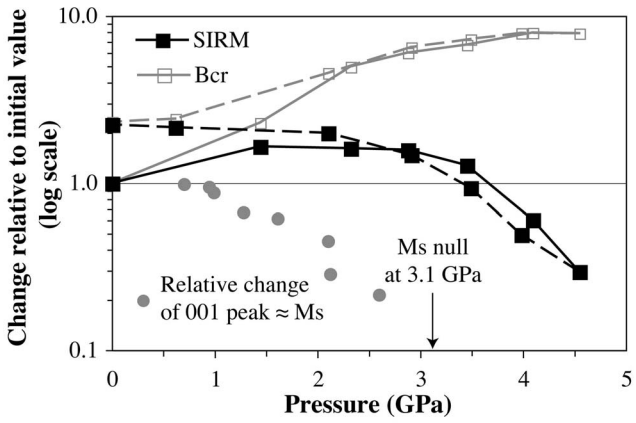

Figure 6. Change relative to initial value for saturation isothermal remanent magnetization (SIRM) and coercivity of remanence (Bcr) for experiment MSM73410–20081215. Gray circles represent the intensity of the (001) ferrimagnetic peak measured with neutron diffraction by *Rochette et al.* [2003]. The signal decreases linearly with pressure from 0.7 to 3.1 GPa following: change relative to initial value = −0.42*pressure (in GPa) + 1.29. As the neutron diffraction data can be used as a proxy for the saturation magnetization (Ms), and the SIRM data is a proxy for the saturation remanent magnetization (Mrs), Mrs/Ms increases upon compression. Decompression paths are indicated by dashed lines.

cannot be attributed solely to pinning effects except upon decompression.

[17] Variability in SIRM moment as a function of pressure is more difficult to understand (Figure 3). To explain the multidomain-rich sample, first we recall cooling experiments on eight multidomain magnetite samples by *Hodych* [1991], who found that Mrs varies in proportion to Bc, compatible with *Néel* [1955] theory for multidomain magnetite. Because Bc of the samples also varied in proportion to their polycrystalline magnetostriction coefficients (λs), *Hodych* [1990, 1991] concluded that changes in Mrs arise from differences in domain wall mobility dictated by the level of internal stress. To test this on pyrrhotite, Figure 5a plots SIRM (remembering that SIRM is equivalent to Mrs) against MDF (remembering that MDF is linearly related to Bc in pyrrhotite); SIRM is again normalized for better comparison. Figure 5b plots relative SIRM versus Bcr. The distinction between the multidomain and single-domain samples becomes immediately clear. As expected, SIRM is invariant with respect to coercivity for single-domain material. At low pressures (<1.5 GPa), the multidomain sample exhibits a positive linear correlation between SIRM and coercivity as predicted. Going higher in pressure, between ~1.5 and 2.8 GPa, SIRM becomes invariant with respect to coercivity; thus, in this pressure regime, the originally multidomain pyrrhotite behaves single domain–like. Interestingly and unexpectedly, a negative correlation between the two emerges at pressures above 2.8 GPa.

[18] Why does a negative correlation arise between SIRM and MDF (and Bcr) at higher pressures? If pyrrhotite had cubic symmetry, one could propose a switch between the easy and hard magnetic axes with a corresponding change in sign of the magnetic anisotropy constants [*Nagata and Kinoshita*, 1965]. Because pyrrhotite has uniaxial symmetry (or potentially triaxial symmetry, but the argument remains the same), and because this uniaxial symmetry becomes more pronounced under pressure, a change in sign of the magnetic anisotropy constant seems unlikely. Does domain wall rotation play a role? In a study of the reversible susceptibility of titanomagnetite as a function of pressure, *Gilder and Le Goff* [2005, Figure 14] found that the magnetic character of four different species of titanomagnetite undergo systematic changes within distinct stress windows. They proposed that a domain production/re-orientation process occurs differently under discrete strain states. *Kean et al.* [1976] also proposed systematic changes in the domain configuration brought about by the application of stress. However, these processes ultimately lead to a steady state domain configuration and one would expect no correlation between SIRM and MDF (i.e., single domain), not a negative one.

[19] To better understand the magnetic properties of pyrrhotite under pressure we plotted the relative changes in SIRM and Bcr from the most complete experiment (MSM73410-20081215) together with the relative intensity of the (001) ferromagnetic peak measured by neutron diffraction as a function of pressure, noting that the (001) peak serves as a proxy for Ms [*Rochette et al.*, 2003] (Figure 6). One must keep in mind that the absolute pressures of the neutron diffraction and magnetometer experiments do not coincide owing to different pressure transmitting media, calibration methods, etc. The relative changes of the hysteresis parameters in Figure 6 allow us to construct idealized hysteresis loops of multidomain pyrrhotite under nonhydrostatic pressure (Figure 7). Ms values were rescaled keeping Ms constant to 1.5 GPa and then decreasing according to the same linear trend defined in Figure 6. Hysteresis loops first become "squarer" and then "squatter" (squat meaning disproportionately broad or wide) with increasing pressure, until they ultimately collapse approaching the paramagnetic transition. Hysteresis loops for single-domain pyrrhotite will follow the same path as for multidomain pyrrhotite except the initial conditions begin farther to the right on Figure 7.

[20] What is the pressure of the phase transition? As described in section 1, previous studies determined the ferromagnetic-to-paramagnetic transition pressure between 1.6 and 6.2 GPa. The broad transition pressure in our study likely arises from the pressure gradient in the cell. Absolute pressure and/or pressure gradients are often not directly measured in the other studies. Moreover, experimental techniques using gamma or X-rays may have further uncertainty depending on where the beams are focused in the cell. Thus, a precise definition of the transition pressure rests ambiguous, with our study falling around 4 ± 1 GPa, in the middle of the published values.

5. Toward a Diamond Pyrrhobarometer

[21] The vast majority of all natural macrodiamonds form within old (>2.5 Ga) continental mantle lithosphere where they are subsequently propelled to the surface in volatile-rich kimberlite magmas. The pressure-temperature conditions estimated from multiple, coexisting inclusions in the

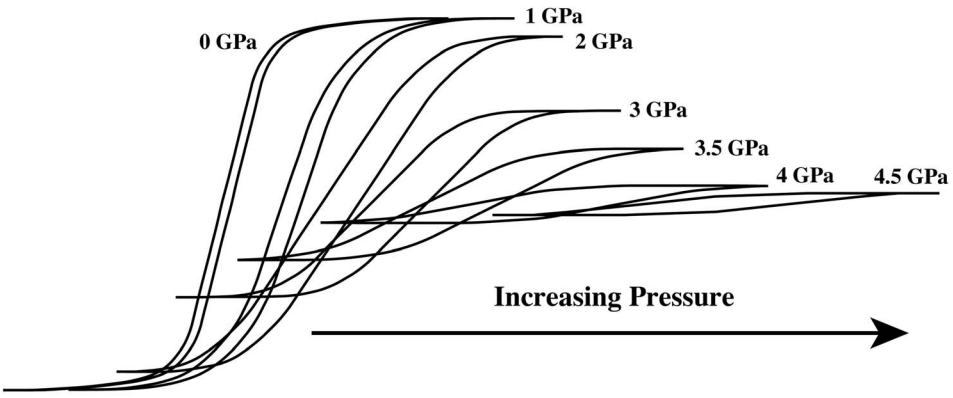

Figure 7. Idealized schematic of magnetic hysteresis loops of multidomain pyrrhotite with increasing pressure. Hysteresis parameters were normalized to initial (0 GPa) conditions following the relative changes shown in Figure 6 as explained in the text. Hysteresis loops for single-domain pyrrhotite will follow the same overall path as for multidomain pyrrhotite, except the initial conditions begin farther to the right.

same diamond places the diamond stability window between temperatures of ~1050 and 1270°C and pressures between 4.3 and 6.5 GPa [*Stachel and Harris*, 2008]. Owing to the differences in thermal expansion and compressibility between pyrrhotite and diamond, pyrrhotite inclusions within diamonds exhumed from mantle depths experience a confining pressure at Earth's surface assuming the diamond is strong enough to contain the pressure. In other words, the pyrrhotite is squeezed as it expands more than the surrounding diamond upon decompression and cooling. If the pressure of the pyrrhotite inclusions exceeds 1 GPa in a host diamond at ambient temperature and pressure, then we can potentially use our experimental results to measure the pressure of the pyrrhotite, and hence unravel the original source pressure of the diamond + pyrrhotite.

[22] The nonreversibility of the individual magnetic parameters seems somewhat unfavorable to develop a geobarometer (see Figures 3c, 3f, and 3g); however, Figure 6 provides encouragement, as the relative change in coercivity and SIRM is the same upon full decompression. We thus plotted Bcr/SIRM and MDF/SIRM for the bulk and normalized values as a function of pressure (Figures 8a–8d), where the results appear quite promising. The similarity of the nonnormalized MDF/SIRM results between the five different experiments must be due to the relatively equal masses of material loaded in the pressure cells seen on a logarithmic scale. Logarithmic plots delineate linear trends for all data above 1 GPa (Figures 8e–8h), with robust correlation coefficients of 0.9. An empirical law establishes that pressure (in GPa) = ln(MDF/SIRM) + 1.

[23] We applied our results to six pyrrhotite-bearing diamonds from a Botswanan kimberlite studied by *Clement et al.* [2008] and one from a placer deposit in the Central African Republic (D21) that we investigated. Anisotropy of isothermal remanent magnetization of the diamonds prompted *Clement et al.* [2008] to measure magnetic hysteresis loops in multiple positions. They found that Mrs values vary up to a factor of 6 and Bc up to a factor of 2.5 in a single diamond, depending on the direction of the applied field relative to the crystallographic axis. For 23 measured hysteresis loops of diamond D21, Mrs varies by a factor of 4 and Bc by 2. We calculated Bc and Mrs from the non-mass-normalized data of each hysteresis loop and plotted Bc/Mrs versus Bc in Figure 9a (data provided by Bradford Clement for the orm [Botswana] diamonds). Despite a positive correlation, much scatter exists in the data, as the mass of pyrrhotite in each diamond is unknown. To get around this problem, we normalized the data by the saturation magnetization (Ms) (i.e., Bc/(Mrs/Ms); see Figure 9b), which results in a more robust correlation. Figure 9b also plots the hysteresis parameters of *Dekkers* [1988] for 12 separate grain-size fractions, ranging from 250 to <5 μm, on two magnetite-free pyrrhotite samples. One clearly observes a departure above Bc values of ~25 mT, with a linear trend defined by varying grain sizes and another by the diamonds. Residual pressure likely explains why the hysteresis parameters of the diamonds lie off the grain-size trend in Figure 9b.

[24] We thus formulated a series of equations to calculate the pressures of the pyrrhotites in the diamonds using the pressure cell experiments (Figure 9c). From Figure 8,

$$P\,(\text{in GPa}) = \ln(\text{MDF/SIRM}) + 1 \text{ and MDF/SIRM} = e^{(P-1)}. \quad (1)$$

From the pressure cell results in Figure 9a,

$$\text{MDF/SIRM} = e^{0.0228\text{MDF}}. \quad (2)$$

Combining equations (1) and (2) yields $e^{0.0228*\text{MDF}} = e^{(P-1)}$, and taking the natural logarithm of both sides gives $0.0228*\text{MDF} = P - 1$, and thus $\text{MDF} = (P - 1)/0.0228$. Recalling again that MDF and SIRM are equivalent to Bc and Mrs in units of mT and Am^2 (or normalized for the latter), respectively. From Figure 9c we obtain

$$\text{BcMs/Mrs} = 35e^{0.0337\text{Bc}}, \quad (3)$$

and after rearranging the terms:

$$\text{BcMs/Mrs} = 35e^{0.0337[(P-1)/0.0228]}. \quad (4)$$

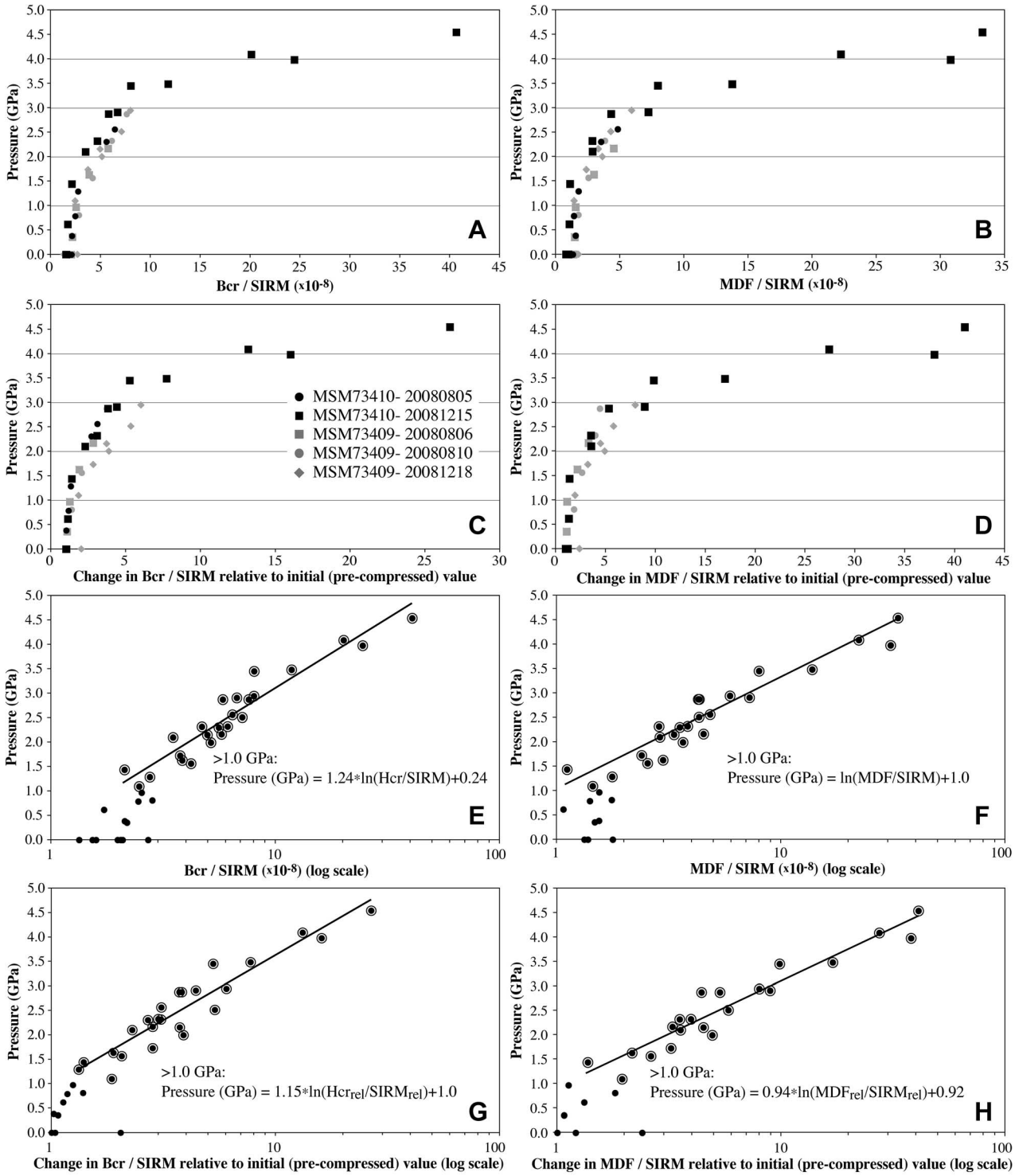

Figure 8. (a and b) Bcr/SIRM and MDF/SIRM versus pressure for all data (compression and decompression) from the five experiments. (c and d) Change in Bcr/SIRM and MDF/SIRM relative to initial (pre-compressed) value versus pressure for all data (compression and decompression) from the five experiments (except 20080805 for MDF). (e–h) Same data as Figures 10a–10d but with a logarithmic scale. Linear segments within different pressure windows and the corresponding equations are fit to all data obtained at pressures >1 GPa (circled points). R^2 values are 0.91 in Figures 8e, 8f, and 8h; 0.89 in Figure 8g.

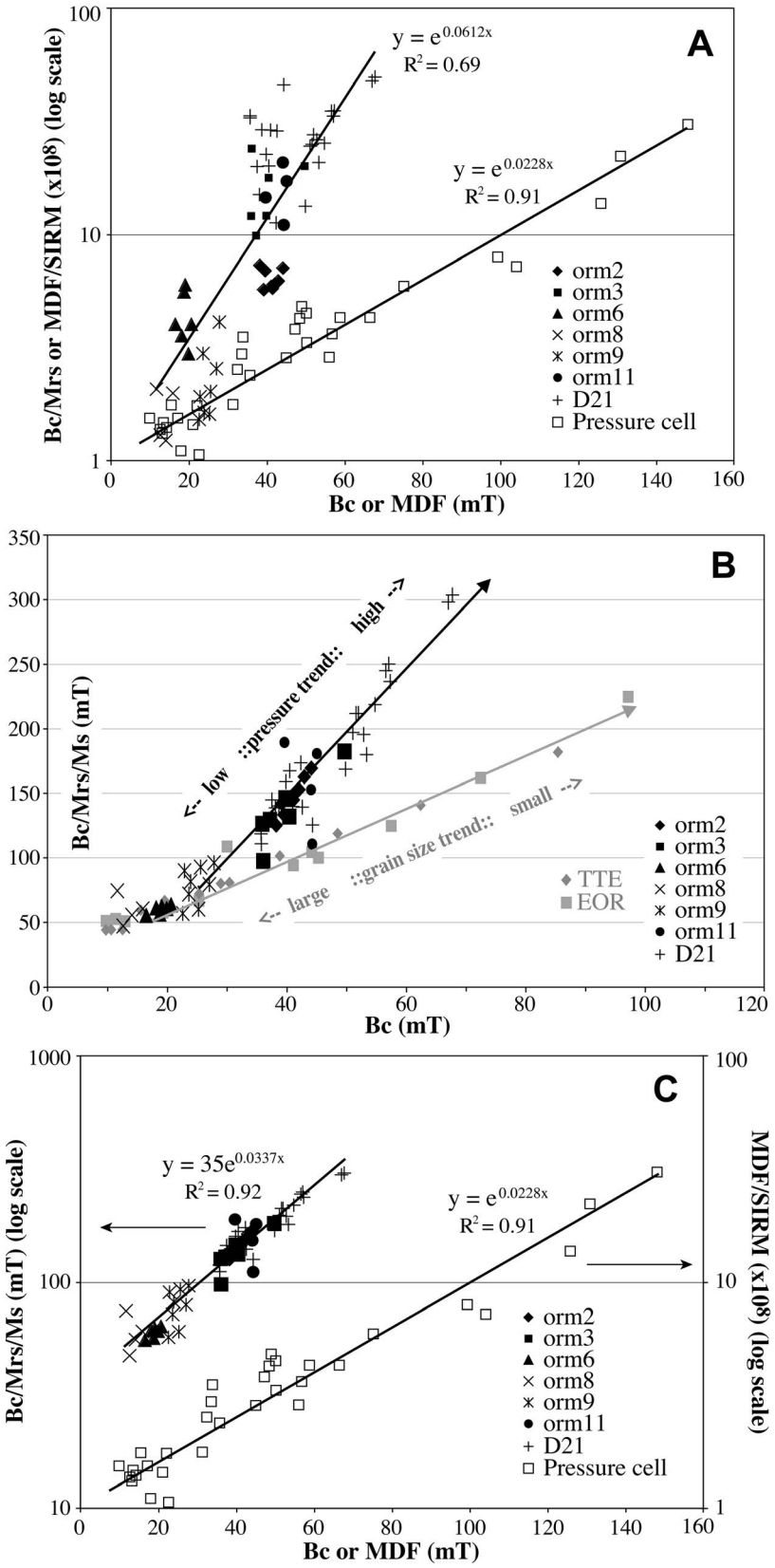
A
y = e^0.0612x
R² = 0.69
y = e^0.0228x
R² = 0.91
Bc/Mrs or MDF/SIRM (x10⁸) (log scale)
Bc or MDF (mT)
orm2
orm3
orm6
orm8
orm9
orm11
D21
Pressure cell
B
Bc/Mrs/Ms (mT)
Bc (mT)
low
::pressure trend::
high
large
::grain size trend::
small
TTE
EOR
C
y = 35e^0.0337x
R² = 0.92
y = e^0.0228x
R² = 0.91
Bc/Mrs/Ms (mT) (log scale)
MDF/SIRM (x10⁸) (log scale)
Bc or MDF (mT)

Figure 9

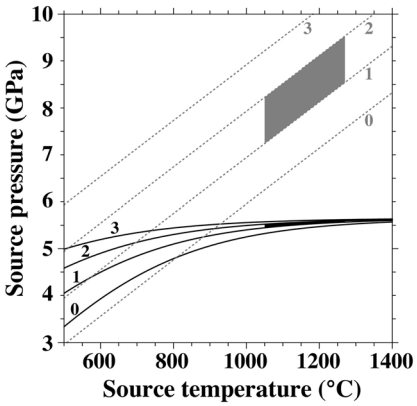

Figure 10. Source pressure and temperature of diamond deduced from pyrrhotite inclusions. Each curve in the plot shows possible source temperature and pressure (x and y axes) stemming from the measured pressure of the pyrrhotite inclusions as indicated by the number (in GPa) near each curve. The filled areas indicate the possible source pressures assuming that the source temperature was between 1050 and 1270°C and given that the measured pressure of pyrrhotite in the host diamond lies between 1 and 2 GPa. The black curves account for the pressure dependence on the thermal expansion coefficient of FeS, while the gray curves ignore it. The latter resemble those for diamond and olivine owing to the small pressure dependency of their thermal expansion coefficients [*Izraeli et al.*, 1999].

Solving equation (4) for pressure:

$$P = \frac{1}{1.478}\ln\left(\frac{BcMs}{35Mrs}\right) + 1 \qquad (5)$$

allows one to calculate the pressure in GPa of pyrrhotite grains under pressure (~>1 GPa) from magnetic hysteresis parameters. After applying equation (5) to the diamonds, we arrive at the following pressure estimates in GPa with 1 σ uncertainties: orm-2, 1.97 ± 0.07; orm-3, 1.91 ± 0.14; orm-6, 1.36 ± 0.04; orm-8, 1.35 ± 0.13; orm-9, 1.54 ± 0.13; orm-11, 1.99 ± 0.16; D21, 2.10 ± 0.19. Despite a ~40% variance about the mean for the hysteresis parameters, the pressure estimates vary less than 10% for an individual diamond. As seen in Figure 9b, diamonds orm-6 and orm-8 lie on the grain-size trend line so assigning overpressure values to those diamonds is highly uncertain. Diamond orm-9 lies at the intersection where the two trends diverge, thus its pressure estimate is ambiguous. However, assigning overpressure values to the rest of the diamonds can be made with relative certainty. This again matches the experimental data where pressures above 1.0 to 1.5 GPa are required for the pressure estimation technique to be valid.

[25] One could directly use the relation P (in GPa) = 0.0228(Bc) + 1 to solve for pressure if one was sure to have multidomain-sized grains as the starting material. Pressures derived from this equation and that of (5) agree to within 5%; interestingly, the two diamonds with the lowest pressures deviate the most. *Clement et al.* [2008] measured the sulphide inclusions in the Botswanan diamonds to be 20 to 50 μm in the largest dimension. Applying P (in GPa) = 0.0228(Bc) + 1 to *Dekkers*' [1988] data suggests that grains larger than 30 μm correspond to apparent pressures less than 1.5 GPa, so without full hysteresis data to demonstrate that a departure from the grain-size trend exists (Figure 9b), one could not distinguish a pressure enhancement of the coercivity versus an apparent pressure due merely to a grain-size effect. If the diamonds contained small single-domain grains, then we would expect the data to be more scattered on Figure 9b, as a combination of grain size and pressure effects would influence the result. Indeed, the linear trend of the diamonds on Figure 9b likely suggests that the pyrrhotite inclusions originated in the multidomain state. The safest way to use the pyrrhotite barometer is on inclusions that are demonstrably multidomain in size (>30 μm).

[26] *Izraeli et al.* [1999] used Raman spectroscopy to measure the internal pressure on olivine inclusions in diamonds from Russia at room temperature. Pressure ranged from 0.13 to 0.65 GPa on the olivine inclusions they studied. Inclusions associated with cracks in the diamonds showed the same Raman shift as crack-free inclusions in the same diamond. After accounting for differences in the isothermal bulk modulus and the thermal expansion coefficients between olivine and diamond, and assuming a mantle residence temperature of 1200°C, the olivine overpressures at room temperature translate into source pressures ranging from 4.4 to 5.2 GPa, within the stability field of diamond. Because the bulk modulus of pyrrhotite is about two thirds of that for olivine and because pyrrhotite's thermal expansion coefficient is roughly ten times greater [e.g., *Gillet et al.*, 1991; *Tenailleau et al.*, 2005], higher overpressures are expected for pyrrhotite than olivine in diamonds at ambient conditions.

[27] One can calculate the source pressure of pyrrhotite and the host diamond by applying the same procedure as *Izraeli et al.* [1999] (Figure 10). The calculations of *Izraeli et al.* [1999] follow those of *Rosenfeld and Chase* [1961] where pressure (P) felt by a pyrrhotite inclusion (i) in a diamond (d) varies as a function of temperature (T) according to their thermal expansion coefficients (α) and bulk modulus (K):

$$\frac{dP}{dT} = \frac{\alpha_i(T,P) - \alpha_d(T,P)}{\frac{1}{K_i(T,P)} - \frac{1}{K_d(T,P)}}. \qquad (6)$$

Figure 9. (a) Magnetic coercivity (Bc, in mT) divided by the remanent saturation magnetization (Mrs, in Am^2) as a function of Bc for pyrrhotite-bearing diamonds from *Clement et al.* [2008, orm series] and this study (D21) together with the experimental results; equations derived from the exponential fits and corresponding R^2 values are shown. Data point from 4.54 GPa not included. (b) Same data from the diamonds as in Figure 9a, except they have been normalized by the saturation magnetization (Ms). The diamond data are compared against hysteresis parameters for two magnetite-free pyrrhotite samples with grain-size fractions ranging from 250 to 5 μm (TTE and EOR from *Dekkers* [1988]). (c) Diamond data from Figure 9b in comparison with the experimental results from Figure 9a shown on a log scale.

For diamond, we assume that $\alpha_d = \alpha_d(T)$ [*Reeber and Wang*, 1996]. For pyrrhotite, $\alpha_i = \alpha_i(T, 0)\alpha_{i,P}(P)$, where $\alpha_i(T, 0)$ is the thermal expansion coefficient at ambient pressure calculated from lattice constant measurements between 88 and 900 K [*Tsatis*, 1987, 1988; *Tenailleau et al.*, 2005]; $\alpha_{i,P}(P)$ accounts for the pressure dependence. This latter coefficient was determined by normalizing *Kusaba et al.* [1998, Figure 6] with $\alpha_{i,P}(0) = 1$. The bulk modulus of diamond varies as $K_d(T, P) = K_{d0}(1\text{-}k_{d,T}T^2)(1 + k_{d,P}P)$, where K_{d0} is the bulk modulus at room pressure, and $k_{d,T}$ and $k_{d,P}$ are temperature and pressure-dependent coefficients following *Zouboulis et al.* [1998, equation (4)] and *Hofmeister and Mao* [2003, Table 1], respectively. Temperature and pressure dependencies of diamond's bulk modulus varies <1%. The same approach is used for a pyrrhotite inclusion: $K_i(T, P) = K_{i0}(1\text{-}k_{i,T}T^2)(1 + k_{i,P}P)$ noting that the large pressure dependence on pyrrhotite's thermal expansion coefficient due to the phase transition bears greatest on the outcome. As both K_{i0} and $k_{i,P}$ are poorly known for pyrrhotite, we took the corresponding values from FeS [*Hofmeister and Mao*, 2003, Table 1]. Here $k_{i,T}$ was calculated from a least squares fit of *Benbattouche et al.* [1989, Figure 1d].

[28] Two end-member solutions arise contingent on how the pressure dependency of the thermal expansion coefficient is taken into account (Figure 10). Black curves in Figure 10 use the pressure dependency on the thermal expansion coefficient of FeS, while gray curves ignore it. The latter curves thus resemble those for diamond and olivine owing to the small (<1%) pressure dependence of their thermal expansion coefficients [*Izraeli et al.*, 1999]. The shaded region in Figure 10 indicates the approximate source pressures assuming that source temperature was between 1050 and 1270°C and given that the measured pressure of pyrrhotite in the host diamond lies between 1.0 and 2.0 GPa. These end-member scenarios yield source pressure estimates from 5.4 to 5.6 GPa (black) and from 7.3 to 9.5 GPa (gray). Considering that these values represent minimum pressure estimates (we cannot exclude the possibility of pressure relaxation due to breakage of the diamond, etc.), they are compatible with theoretical and experimental constraints on the formation pressure of diamond.

6. Conclusions

[29] We determined the pressure dependency of the magnetic properties of well-characterized, single-domain and multidomain pyrrhotite at room temperature. Repeat experiments yield reproducible results despite differences in degree of nonhydrostaticity. Magnetic coercivity increases as a function of pressure regardless of domain state. Below ~1.5 GPa, the magnetization and coercivity of single-domain pyrrhotite are uncorrelated owing to the invariability of its magnetization, whereas multidomain pyrrhotite exhibits a positive linear correlation between magnetization and coercivity, compatible with Néel theory. From ~1.5 to ~2.8 GPa, multidomain pyrrhotite behaves single domain–like, yet different from noncompressed single-domain pyrrhotite, which we attribute to an increase in magnetocrystalline anisotropy (magnetostriction) in combination with the complete pinning of domain walls. Above ~2.8 GPa, approaching the phase transition, a new state is reached where magnetization and coercivity are negatively correlated until complete disruption of magnetic exchange likely occurs. These observations led us to establish an empirical model of the effect of pressure on pyrrhotite's magnetic properties. Above ~1 GPa, pyrrhotite's magnetic coercivity normalized to its magnetization varies logarithmically as a function of pressure, opening the possibility for its use as a geobarometer. Application of this potential geobarometer to pyrrhotite-bearing diamonds yields reasonable estimates for diamond formation pressures. Moreover, data acquisition takes only about five minutes with minimal sample preparation and is nondestructive. Performance of the pyrrhotite geobarometer can be improved with better knowledge of pyrrhotite's elastic constants at high pressures and high temperatures and through further experimentation at high pressures under different degrees of (non)hydrostaticity. A pyrrhotite-based barometer could be used in combination with Raman spectrometry to examine the consistency between methods in estimating diamond formation pressures. Using high-energy X-rays, one could measure the lattice parameters of the pyrrhotite in the diamond to assess their overpressures and compare with the magnetically constrained value. As pyrrhotite is found in meteorites, perhaps a barometer can be established in combination with other host minerals.

[30] **Acknowledgments.** We thank Mark Dekkers, Wim van Westrenen, and an anonymous reviewer for their very helpful and insightful comments. Brad Clement kindly provided the raw hysteresis data for the orm diamonds. This work was financed by Deutsche Forschungsgemeinschaft grant GI712/7-1.

References

Adams, D., R. Appleby, and S. Sharma (1976), Spectroscopy at very high pressures: Part X. Use of ruby R-lines in the estimation of pressure at ambient and at low temperatures, *J. Phys. E Sci. Instrum.*, *9*, 1140–1144, doi:10.1088/0022-3735/9/12/034.

Ahrens, T. J. (1979), Equations of state of iron sulfide and constraints on the sulfur-content of the Earth, *J. Geophys. Res.*, *84*, 985–998, doi:10.1029/JB084iB03p00985.

Arnold, R. G. (1967), Range in composition and structure of 82 natural terrestrial pyrrhotites, *Can. Mineral.*, *9*, 31–50.

Benbattouche, N., G. A. Saunders, E. F. Lambson, and W. Hönle (1989), The dependencies of the elastic stiffness moduli and the Poisson ratio of natural iron pyrites FeS_2 upon pressure and temperature, *J. Phys. D Appl. Phys.*, *22*, 670–675, doi:10.1088/0022-3727/22/5/015.

Bertaut, E. F. (1953), Contribution à l'étude des structures lacunaires—La pyrrhotine, *Acta Crystallogr.*, *6*, 557–561, doi:10.1107/S0365110X53001502.

Bezaeva, N., J. Gattacceca, P. Rochette, R. Sadykov, and V. Trukhin (2010), Demagnetization of terrestrial and extraterrestrial rocks under hydrostatic pressure up to 1.2 GPa, *Phys. Earth Planet. Inter.*, *179*, 7–20, doi:10.1016/j.pepi.2010.01.004.

Bin, M., and R. Pauthenet (1963), Magnetic anisotropy in pyrrhotite, *J. Appl. Phys.*, *34*, 1161–1162, doi:10.1063/1.1729413.

Buddhue, J. D. (1945), Some meteoritic iron sulfides, *Pop. Astron.*, *53*, 405–408.

Chervin, J. C., B. Canny, and M. Mancinelli (2001), Ruby-spheres as pressure gauge for optically transparent high pressure cells, *High Pressure Res.*, *21*, 305–314, doi:10.1080/08957950108202589.

Clement, B. M., S. Haggerty, and J. Harris (2008), Magnetic inclusions in diamonds, *Earth Planet. Sci. Lett.*, *267*, 333–340, doi:10.1016/j.epsl.2007.11.052.

Collinson, D. W. (1986), Magnetic properties of Antarctic shergottite meteorites EET A79001 and ALH A77005: Possible relevance to a Martian magnetic field, *Earth Planet. Sci. Lett.*, *77*, 159–164, doi:10.1016/0012-821X(86)90157-3.

Dankers, P. (1981), Relationship between median destructive field and remanent coercive forces for dispersed natural magnetite, titanomagnetite and hematite, *Geophys. J. R. Astron. Soc.*, *64*, 447–461.

Dekkers, M. J. (1988), Magnetic-properties of natural pyrrhotite 1. Behavior of initial susceptibility and saturation-magnetization-related rock-magnetic parameters in a grain-size dependent framework, *Phys. Earth Planet. Inter.*, *52*, 376–393, doi:10.1016/0031-9201(88)90129-X.

Dekkers, M. J. (1989), Magnetic-properties of natural pyrrhotite 2. High-temperature and low-temperature behavior of Jrs and TRM as function of grain-size, *Phys. Earth Planet. Inter.*, *57*, 266–283, doi:10.1016/0031-9201(89)90116-7.

Dekkers, M. J., J. L. Mattei, G. Fillion, and P. Rochette (1989), Grain-size dependence of the magnetic behavior of pyrrhotite during its low-temperature transition at 34 K, *Geophys. Res. Lett.*, *16*, 855–858, doi:10.1029/GL016i008p00855.

Dunlop, D. J., and J. Arkani-Hamed (2005), Magnetic minerals in the Martian crust, *J. Geophys. Res.*, *110*, E12S04, doi:10.1029/2005JE002404.

Gilder, S., and M. Le Goff (2005), Pressure dependence on the magnetic properties of titanomagnetite using the reversible susceptibility method, in *Advances in High-Pressure Technology for Geophysical Applications*, edited by J. H. Chen et al., pp. 315–335, Elsevier, Amsterdam, doi:10.1016/B978-044451979-5/50017-X.

Gilder, S., and M. Le Goff (2008), Systematic pressure enhancement of titanomagnetite magnetization, *Geophys. Res. Lett.*, *35*, L10302, doi:10.1029/2008GL033325.

Gilder, S., M. Le Goff, J. Peyronneau, and J. C. Chervin (2004), Magnetic properties of single and multi-domain magnetite under pressures from 0 to 6 GPa, *Geophys. Res. Lett.*, *31*, L10612, doi:10.1029/2004GL019844.

Gillet, P., P. Richet, F. Guyot, and G. Fiquet (1991), High-temperature thermodynamic properties of forsterite, *J. Geophys. Res.*, *96*, 11,805–11,816, doi:10.1029/91JB00680.

Halgedahl, S. L., and M. Fuller (1981), The dependence of magnetic domain-structure upon magnetization state in polycrystalline pyrrhotite, *Phys. Earth Planet. Inter.*, *26*, 93–97, doi:10.1016/0031-9201(81)90101-1.

Haraldsen, H. (1937), Eine thermomagnetische untersuchung der umwandlungen im troilit-pyrrhotin-gebiet des eisen-schwefel-systems, *Z. Anorg. Allg. Chem.*, *231*, 78–96, doi:10.1002/zaac.19372310110.

Haraldsen, H. (1941), Uber die Eisen (II)-Sulfidmischkristalle, *Z. Anorg. Allg. Chem.*, *246*, 169–194, doi:10.1002/zaac.19412460206.

Hayase, K., R. Otsuka, and T. Mariko (1963), On the magnetic properties of natural pyrrhotites, *Mineral. J.*, *4*, 41–56.

Hodych, J. P. (1990), Magnetic hysteresis as a function of low-temperature in rocks—Evidence for internal-stress control of remanence in multidomain and pseudo-single-domain magnetite, *Phys. Earth Planet. Inter.*, *64*, 21–36, doi:10.1016/0031-9201(90)90003-G.

Hodych, J. P. (1991), Low-temperature demagnetization of saturation remanence in rocks bearing multidomain magnetite, *Phys. Earth Planet. Inter.*, *66*, 144–152, doi:10.1016/0031-9201(91)90073-Q.

Hofmeister, A. M., and H. K. Mao (2003), Pressure derivatives of shear and bulk moduli from the thermal Grüneisen parameter and volume-pressure data, *Geochim. Cosmochim. Acta*, *67*, 1215–1235, doi:10.1016/S0016-7037(02)01289-9.

Hurlbut, C. S., Jr., and C. Klein (1977), *Manual of Mineralogy*, John Wiley, New York.

Izraeli, E. S., J. W. Harris, and O. Navona (1999), Raman barometry of diamond formation, *Earth Planet. Sci. Lett.*, *173*, 351–360, doi:10.1016/S0012-821X(99)00235-6.

Jeandey, C., J. L. Oddou, J. L. Mattei, and G. Fillion (1991), Mössbauer investigation of the pyrrhotite at low temperature, *Solid State Commun.*, *78*, 195–198, doi:10.1016/0038-1098(91)90282-Z.

Kamimura, T., M. Sato, and H. Takahashi (1992), Pressure-induced phase-transition in Fe-Se and Fe-S systems with a NiAs-type structure, *J. Magn. Magn. Mater.*, *104–107*, 255–256, doi:10.1016/0304-8853(92)90787-O.

Kean, W., R. Day, M. Fuller, and V. Schmidt (1976), The effect of uniaxial compression on the initial susceptibility of rocks as a function of grain size and composition of their constituent titanomagnetites, *J. Geophys. Res.*, *81*, 861–872, doi:10.1029/JB081i005p00861.

Kobayashi, H., M. Sato, T. Kamimura, M. Sakai, H. Onodera, N. Kuroda, and Y. Yamaguchi (1997), The effect of pressure on the electronic states of FeS and Fe_7S_8 studied by Mössbauer spectroscopy, *J. Phys. Condens. Matter*, *9*, 515–527, doi:10.1088/0953-8984/9/2/019.

Kusaba, K., Y. Syono, T. Kikegawa, and O. Shimomura (1998), High pressure and temperature behavior of FeS, *J. Phys. Chem. Solids*, *59*, 945–950, doi:10.1016/S0022-3697(98)00015-8.

Laves, F. (1930), Die bau-zusammenhänge innerhalb der kristallstrukturen, *Zeit. Kristallogr. Miner.*, *73*, 275–324.

Louzada, K. L., S. T. Stewart, and B. P. Weiss (2007), Effect of shock on the magnetic properties of pyrrhotite, the Martian crust, and meteorites, *Geophys. Res. Lett.*, *34*, L05204, doi:10.1029/2006GL027685.

Louzada, K. L., S. T. Stewart, B. P. Weiss, J. Gattacceca, and N. S. Bezaeva (2010), Shock and static pressure demagnetization of pyrrhotite and implications for the Martian crust, *Earth Planet. Sci. Lett.*, *290*, 90–101, doi:10.1016/j.epsl.2009.12.006.

Morimoto, N., A. Gvobu, K. Tsukuma, and K. Koto (1975), Superstructure and non-stoichiometry of intermediate pyrrhotite, *Am. Mineral.*, *60*, 240–248.

Nagata, T., and H. Kinoshita (1965), Studies on Piezo-magnetization (I) magnetization of titaniferous magnetite under uniaxial compression, *J. Geomagn. Geoelectr.*, *17*, 121–135, doi:10.5636/jgg.17.121.

Néel, L. (1952), Antiferromagnetism and ferrimagnetism, *Proc. Phys. Soc. London*, *65*, 869–885, doi:10.1088/0370-1298/65/11/301.

Néel, L. (1955), Some theoretical aspects of rock-magnetism, *Adv. Phys.*, *4*, 191–243, doi:10.1080/00018735500101204.

Pouchou, J. L., and F. Pichoir (1984), Un nouveau modèle de calcul pour la microanalyse quantitative par spectrométrie de rayons X. partie I: Application à l'analyse des échantillons homogènes, *Rech. Aerosp.*, *3*, 167–192.

Reeber, R. R., and K. Wang (1996), Thermal expansion, molar volume, and specific heat of diamond from 0 to 3000 K, *J. Electron. Mater.*, *25*, 63–67, doi:10.1007/BF02666175.

Rochette, P., G. Fillion, J. L. Mattei, and M. J. Dekkers (1990), Magnetic transition at 30–34 Kelvin in pyrrhotite—Insight into a widespread occurrence of this mineral in rocks, *Earth Planet. Sci. Lett.*, *98*, 319–328, doi:10.1016/0012-821X(90)90034-U.

Rochette, P., G. Fillion, R. Ballou, F. Brunet, B. Ouladdiaf, and L. Hood (2003), High pressure magnetic transition in pyrrhotite and impact demagnetization on Mars, *Geophys. Res. Lett.*, *30*(13), 1683, doi:10.1029/2003GL017359.

Rochette, P., J. Gattacceca, V. Chevrier, V. Hoffmann, J.-P. Lorand, M. Funaki, and R. Hochleitner (2005), Matching Martian crustal magnetization and magnetic properties of Martian meteorites, *Meteorit. Planet. Sci.*, *40*, 529–540, doi:10.1111/j.1945-5100.2005.tb00961.x.

Rosenfeld, J. L., and A. B. Chase (1961), Pressure and temperature of crystallization from elastic effects around solid inclusions in minerals, *Am. J. Sci.*, *259*, 519–541, doi:10.2475/ajs.259.7.519.

Schwarz, E. J., and D. J. Vaughan (1972), Magnetic phase relations of pyrrhotite, *J. Geomagn. Geoelectr.*, *24*, 441–458, doi:10.5636/jgg.24.441.

Soffel, H. C. (1981), Domain-structure of natural fine-grained pyrrhotite in a rock matrix (diabase), *Phys. Earth Planet. Inter.*, *26*, 98–106, doi:10.1016/0031-9201(81)90102-3.

Stachel, T., and J. W. Harris (2008), The origin of diamonds—Constraints from mineral inclusions, *Ore Geol. Rev.*, *34*, 5–32, doi:10.1016/j.oregeorev.2007.05.002.

Tenailleau, C., B. Etschmann, H. Wang, A. Pring, B. A. Grguric, and A. Studer (2005), Thermal expansion of troilite and pyrrhotite determined by in situ cooling (873 to 373 K) neutron powder diffraction measurements, *Mineral. Mag.*, *69*, 205–216, doi:10.1180/0026461056920247.

Tsatis, D. (1987), Thermal expansion of pyrrhotite (Fe_7S_8), *J. Phys. Chem. Solids*, *48*, 489–490, doi:10.1016/0022-3697(87)90110-7.

Tsatis, D. (1988), Thermal expansion of pyrrhotite (Fe_7S_8) at high temperatures, *J. Phys. Chem. Solids*, *49*, 359–362, doi:10.1016/0022-3697(88)90092-3.

Vaughan, D. J., and M. S. Ridout (1970), Mössbauer study of pyrrhotite, *Solid State Commun.*, *8*, 2165–2167, doi:10.1016/0038-1098(70)90242-5.

Vaughan, D. J., and J. A. Tossell (1973), Magnetic transitions observed in sulfide minerals at elevated pressures and their geophysical significance, *Science*, *179*, 375–377, doi:10.1126/science.179.4071.375.

Worm, H. U., D. Clark, and M. J. Dekkers (1993), Magnetic-susceptibility of pyrrhotite—Grain size, field and frequency-dependence, *Geophys. J. Int.*, *114*, 127–137, doi:10.1111/j.1365-246X.1993.tb01472.x.

Zapletal, K. (1993), Effect of intergrowths of the ferrimagnetic and antiferromagnetic phases on the rock magnetic-properties of natural pyrrhotites, *Phys. Earth Planet. Inter.*, *76*, 151–162, doi:10.1016/0031-9201(93)90064-G.

Zouboulis, E. S., M. Grimsditch, A. K. Ramdas, and S. Rodriguez (1998), Temperature dependence of the elastic moduli of diamond: A Brillouin-scattering study, *Phys. Rev. B*, *57*, 2889–2896, doi:10.1103/PhysRevB.57.2889.

M. de Wit, Africa Earth Observatory Network, Nelson Mandela Metropolitan University, PO Box 77000, Port Elizabeth 6031, South Africa. (maarten.dewit@nmmu.ac.za)

R. Egli, S. A. Gilder, S. C. Roud, and M. W. R. Volk, Department of Earth and Environmental Sciences, Ludwig Maximilians University, Theresienstr. 41, D-80333 Munich, Germany. (gilder@lmu.de)

R. Hochleitner, Mineralogische Staatssammlung München, Theresienstr. 41, D-80333 Munich, Germany.

M. Le Goff, Laboratoire du Paléomagnétisme, Institut de Physique du Globe, F-75252 Paris Cedex 05, France.